

# Near-Source Ground Motion Estimation for Assessing the Seismic Hazard of Critical Facilities in Central Italy

Luca Moratto (✉ [lmoratto@ogs.it](mailto:lmoratto@ogs.it))

National Institute of Oceanography and Experimental Geophysics: Istituto Nazionale di Oceanografia e Geofisica Sperimentale <https://orcid.org/0000-0001-6328-2138>

**Marco Santuillin**

National Institute of Oceanography and Experimental Geophysics: Istituto Nazionale di Oceanografia e Geofisica Sperimentale

**Alberto Tamaro**

National Institute of Oceanography and Experimental Geophysics: Istituto Nazionale di Oceanografia e Geofisica Sperimentale

**Angela Saraò**

National Institute of Oceanography and Experimental Geophysics: Istituto Nazionale di Oceanografia e Geofisica Sperimentale

**Alessandro Vuan**

National Institute of Oceanography and Experimental Geophysics: Istituto Nazionale di Oceanografia e Geofisica Sperimentale

**Alessandro Rebez**

National Institute of Oceanography and Experimental Geophysics: Istituto Nazionale di Oceanografia e Geofisica Sperimentale

---

## Research Article

**Keywords:** Near-source, seismic hazard, ground motion variability, vertical component, seismic input, critical facilities

**Posted Date:** May 31st, 2022

**DOI:** <https://doi.org/10.21203/rs.3.rs-1664691/v1>

**License:** © ⓘ This work is licensed under a Creative Commons Attribution 4.0 International License.

[Read Full License](#)

---

# Abstract

We apply the Probabilistic Seismic Hazard Analysis (PSHA) and Deterministic Seismic Hazard Analysis (DSHA) to estimate the input ground motion for three dams in the Campotosto area (Central Italy). The dams, which confine an artificial water reservoir feeding hydroelectric power plants, are located in an active seismic zone between the areas that experienced the 2009 L'Aquila and 2016–2017 Central Italy seismic sequences. The probabilistic disaggregation estimated for a return period of 2475 years, corresponding to the collapse limit state for critical facilities, indicates that the most dangerous fault is associated with a maximum magnitude of  $6.75 \pm 0.25$  within a distance of 10 km. This fault is used in DSHA to emulate the worst-case scenario. To capture the ground motion variability, we input a pseudo-dynamic source model to encompass spatial and temporal variations in the slip, rise time and rupture propagation, heavily affecting the near-source ground motion. Indeed, the ground motion above the rupture volume is mainly influenced by the epistemic uncertainties of rupture nucleation and slip distribution. The computed broadband seismograms are consistent with the near-source shaking recorded during the 2016  $M_W$  6.6 Norcia earthquake and constrain the upper bound of the simulated ground motion at specific sites. Our modelling reinforces the importance of considering vertical ground motion near the source in seismic design. It could reach shaking values comparable to or larger than those of the horizontal components.

This approach can be applied in other areas with high seismic hazard to evaluate the seismic safety of existing critical facilities.

## 1. Introduction

Seismic hazard quantifies the ground motion expected at a particular site and provides the seismic parameters needed to mitigate earthquake damage. Detailed hazard estimates are routinely performed for critical facilities such as nuclear power plants, dams, gas storage, and pipelines using probabilistic or deterministic approaches or integrating both (e.g., Renault, 2014; Dello Russo et al., 2017; Tamaro et al., 2018; Slejko et al., 2021; Moratto et al., 2021).

The Probabilistic Seismic Hazard Analysis (PSHA) (Cornell, 1968) is currently the standard approach required by the Italian seismic code and is widely used for spatial and punctual planning strategies. The PSHA simulates the ground motion by systematically integrating all possible seismic source models obtained from joint seismological and geological information for a given area. It estimates the probability that various levels of earthquake-caused ground motions will be exceeded at a given location in a given time. The Deterministic Seismic Hazard Analysis (DSHA) evaluates the strong ground motion at selected sites for a specific earthquake scenario (or a combination of earthquakes), generally the worst-case scenario. It can enrich the near-source information where the source effects dominate, and strong motion records may be missing. Common to both approaches is the fundamental issue of identifying potential sources of earthquakes (Bommer, 2002). However, determinism versus probabilism should be a continuum where both analyses are conducted (McGuire, 2001; Bommer, 2002). PSHA can be applied for

evaluations in the broader area, while DSHA can be adopted for the detailed design of critical structures based on the controlling earthquake (Krinitzsky, 2003). The disaggregation of PSHA is an essential tool in these hybrid approaches to identify the most dangerous source (Bommer, 2002).

This study integrates PSHA and DSHA to estimate the seismic input for the hazard assessment in an active seismic zone of Campotosto (Central Italy), an area hosting the second-largest artificial water reservoir in Europe bordered by three dams and hydroelectric power plants (Fig. 1). Strong earthquakes struck the zone in 1619 and 1672, and other related earthquakes occurred in 1639 and 1703 (Rovida et al., 2020). The area is located between the 2009 L'Aquila sequence ( $M_w$  6.3), related to the Paganica fault (e.g. Chiarabba et al., 2009) and the 2016–2017 Central Italy seismic sequence (e.g. Chiaraluce et al., 2017; Vuan et al., 2017; 2018), dominated by three mainshocks ( $M_w$  6.2, on August 24 2016;  $M_w$  6.1, on October 26 2016;  $M_w$  6.6, on October 30 2016) and activating the Mt. Vettore-Mt. Bove fault system (e.g. Falcucci et al., 2018). These sequences occurred on NW-SE striking faults (ITHACA, 2019), SW dipping and aligned to the system of normal faults along the Apennine chain (Falcucci et al., 2018).

Paleoseismology evidenced significant surface-rupturing events capable of triggering an  $M > 6.5$  earthquake (Galadini and Galli, 2003) in the Campotosto area, where Falcucci et al. (2018) estimated a possible earthquake in the range  $M_w$  6.4–6.6, making this area one of the most problematic seismic gaps of Central Italy. Tondi et al. (2021) suggested that the seismogenic potential of this zone is in the order of  $M_w=6.0$ . The Campotosto area was affected by the migration of the seismicity in 2009 toward North from L'Aquila and in 2017 toward South from Amatrice; these seismic activities caused multiple moderate earthquakes ( $M_w \leq 5.5$ ) nucleated in the Campotosto area.

Several studies estimated the PSHA in the area of Campotosto (e.g. Meletti et al., 2006; Stucchi et al., 2011; Woessner et al., 2015; Martelli et al., 2017; Santulin et al., 2017); although the zonations used in these studies are similar, different Ground Motion Models (GMM) led to a generalized increase in the PSHA values. GMM are widely used in seismic hazard, but they are not well constrained in the near-source (e.g. Mai, 2009; Sgobba et al. 2021) because the data representativity is not statistically significant at short source distances, particularly for normal faults (e.g. Valentova et al., 2021). Although recent GMM (e.g. Spudich et al., 2014) consider finite-fault effects (e.g. focal mechanism, directivity), the ergodic assumption, the unsatisfactory integration of spatial correlation, and the lack of data in the near-source poorly constrain the near-source ground motion prediction accuracy (e.g. Pischiutta et al., 2021; Xin and Zhang, 2021). Therefore, physics-based numerical simulations could be preferable when the source and the propagation processes are known to capture better the spatial variation of the near-source ground motion. The GMM can be used to preliminarily judge the reasonability of DSHA scenarios (Xin and Zhang, 2021). Considering finite fault effects to simulate ground motion in near-source is essential for seismic hazard assessment and infrastructure design. Indeed, too simplified models based on isotropic assumptions may represent a strong oversimplification in near-source and could be unreliable for assessing the seismic risk of critical facilities (Schiappapietra and Smerzini, 2021).

In the following, after describing the PSHA conducted in this study, we estimate the seismic potential of active faults and related epistemic uncertainties of PSHA parameters, identifying the most dangerous seismic source for the dams. Such a source is used in the DSHA to model the worst-case scenario by computing the ground motion for three near-source receivers located at the three dams along the edges of the Campotosto Lake. We provide synthetic broadband waveforms and spectral parameters that can be used as input motion for the seismic design and retrofitting in the area.

## 2. Probabilistic Seismic Hazard

We evaluate the PSHA of the Campotosto region by modelling fault sources. The code used is Openquake (Pagani et al., 2014), which provides hazard curves for the desired Ground Motion Model (GMM), and uniform hazard response spectra (UHRS) for selected sites. The fault model is based on the 3-D fault system given in the Fault2SHA Central Apennines Database (CAD) (Faure Walker et al., 2020); rupture rates are parameterized by using the SHERIFS code (Chartier et al., 2019) that allows seismic ruptures involving multiple sections of a single fault or interactions between multiple faults.

The Fault2SHA code CAD (Faure Walker et al., 2020) brings together the knowledge of field geologists and seismic hazard modellers, and facilitates the definition of PSHA uncertainties.

The SHERIFS code requires the faults' geometries and the slip rates to calculate rupture rates. Given a fixed shape of the magnitude-frequency distribution (MFD) set for the entire fault system (target MFD), its iterative procedure establishes all possible earthquake rupture scenarios in the area. At each iteration, a magnitude is randomly selected based on the target MFD, and an earthquake rupture scenario that generates that magnitude is selected. For this scenario, an increase in the slip-rate budget of the affected faults is converted into an earthquake rupture rate for the magnitude under consideration. At the beginning of the iterative process, only the shape of the target MFD is set without knowing its absolute value. The iterative computation continues until the fault slip-rate budget is exhausted. The code compares the modelled earthquake rates with the local earthquake catalogue. We use for this comparison the rates based on the declustered Parametric Catalogue of Italian Earthquakes (Rovida et al., 2019; 2020) and the completeness periods of Meletti et al. (2019).

We started by defining the limits of the fault system in an area of about 100 km around Campotosto Lake (Fig. 1). Since the Fault2SHA CAD (Faure Walker et al., 2020) database does not cover the northern part of the study area, we integrated the system with the individual seismogenic sources of the DISS 3.2.1 catalogue (DISS Working Group, 2018), collecting all the information needed by SHERIFS: the geometry (trace, dip and upper and lower seismogenic depth), the slip rate with uncertainties and the kinematics (normal, strike slip, reverse or rake) of the fault sections. We defined the length of the fault sections in order of the dimensions of the seismogenic depth, which was set at 10 km. Faults with a longer length are divided into smaller sections (however, smaller sections can break together). We have assumed that the seismicity of the complete fault system follows the form of a Gutenberg and Richter (1944) type distribution.

We have analysed the uncertainties associated with the fault slip rate, the magnitude scale parameters, and the b-value. In SHERIFS, the uncertainty limits are defined and explored based on the number of user-defined random samples, which in our case were set to 20, each representing a model for each branch of the logic tree (see the electronic supplement Fig. ES1). For each model, a slip-rate value is chosen uniformly within the uncertainty limits associated with each fault in the database; the scale law parameters are independently selected according to a Gaussian distribution within their error limits, and a b-value is set within the range considered by the user, in our case 0.9–1.1. The uncertainties of the two magnitude scale relationships (Wells and Coppersmith, 1994; Leonard, 2010) in estimating the  $M_{\max}$  are accounted for by random sampling of the two-scale relations.

In summary, to account for the epistemic uncertainties, we implemented a logic tree of 120 branches, as shown in Fig. 2: the fault model is unique, as described previously; two magnitude-rupture scaling relationships (W&C94, Wells and Coppersmith, 1994 and Leo10, Leonard, 2010) to calculate the maximum magnitude each fault can accommodate, based on the rupture area for normal faults; twenty random samples within the lower and upper bounds of a centred triangular distribution to explore the epistemic uncertainty of 1) the b-value of the target MFD for the fault network, 2) the maximum magnitude ( $M_{\max}$ ) due to the uncertainty in the scaling law and 3) the slip rates of the faults. Also, we use the three GMMs with the highest weights selected by Lanzano et al. (2020) to compute the new Italian seismic hazard map: the Cauzzi et al. (2015), the Bindi et al. (2014), and the Bindi et al. (2011) calibrated on a global, European and Italian database, respectively.

To assess the seismic hazard of the Campotosto Lake area, we use the synthetic seismicity rates resulting from the SHERIFS' computations as input for the Openquake code (Pagani et al., 2014), using the specific codes of Scotti et al. (2021). In this study, we did not analyze the influence of the different soils and considered the whole area as bedrock ( $V_{s30} > 800\text{m/s}$ ).

The most common result of a hazard analysis is the hazard curve, which represents the annual probability of exceeding certain shaking levels (Kramer, 1996) in a fixed period. From the hazard curves obtained for PGA and response spectra computed at different spectral ordinates (e.g. 0.1s, 1s...), it is possible to obtain the uniform hazard response spectra, which have the same probability of exceeding, at all frequencies, for a fixed return period. The Campotosto hazard curves for both the horizontal and vertical components are shown in Fig. 3a and 3b: the dispersion of the individual branches of hazard curves is linked to the different epistemic uncertainties analysed.

Figures 3c and 3d illustrate the horizontal UHRS for the 2475 and 475 years return periods, respectively, obtained from the different GMMs, while Figs. 3e and 3f refer to the vertical components, for which only the Bindi et al. (2011) model is available. The obtained mean and different quantiles spectra are also represented as the weighted average of the various individual spectra of the logic tree. When analysing the logic tree branches, a strong dispersion is noted in PGA, maximum spectral acceleration, and the corresponding period for the horizontal components. The numerical results and the shape of the curve are strongly influenced by the branches of the Cauzzi et al. (2015) model.

In a classical PSHA, all earthquakes contribute to building the seismic hazard of a site. In our analysis, we obtain the scenario that most affects the hazard of a site, expressed in terms of magnitude-distance pair, by disaggregating the probabilistic calculation. The disaggregation allows us to identify, among all the earthquakes considered to compute the seismic hazard of a region, the one that contributes most (McGuire, 1995).

For a 2475 years return period (see the electronic supplement Fig. ES2a), the magnitude-distance pair that most affects the hazard of a site within the first 10 km of distance is  $M_W 6.75 \pm 0.25$ , whereas for a 475 years return period (see the electronic supplement Fig. ES2b), it is  $M_W 5.25 \pm 0.25$ . To evaluate the contribution of each fault section to the hazard, we computed PGA curves for each rupture scenario at the site. The sum of all these hazard curves gives the total hazard at the site (Fig. 4a). The slip values of the fault sections included in the seismic hazard computation are shown in Fig. 4b.

The contribution of each section to the hazard of Campotosto is obtained by summing its hazard curves for each rupture scenario in which it is involved, normalizing the sum to the total hazard curve. Figure 5a shows, for each PGA level, the sections contributing to the probability of exceedance (POE) of that PGA level. In Fig. 5b, we map the contribution of the sections to hazard at the Campotosto site (PGA 0.816 g) and surrounding area, obtained for the 2475 years return period: the hazard is mainly influenced by the nearest sections around our study site (Laga, Assergi and Barisciano sections) with similar contribution, while, for lower PGA levels, the Laga sections become prevalent (Fig. 5a), even if they are not in the highest slip rate classes (Fig. 4b). This is due to the close distance of these sections to the site. This is a significant result obtained from mapping hazard based on faults, compared to seismotectonic zoning approaches that smooth out the hazard in large zones, ignoring local information on active faults.

### 3. Deterministic Seismic Hazard

#### 3.1 Broadband simulations using the pseudo-dynamic approach

The DSHA ground motion is computed by applying COMPEX (Moratto et al., 2015; 2021), a hybrid approach to computing broadband seismograms combining the time series calculated in the low-frequency range by COMPSYN deterministic code (Spudich and Xu, 2003) with the stochastic signals calculated in the high-frequency by EXSIM (Motazedian and Atkinson, 2005; Boore, 2009). The Fourier amplitude spectra of the computed velocity seismograms are merged by applying the matching filters at the intersection frequency; after that, the stochastic spectra are scaled on the deterministic spectra to reduce artificial spectral steps as described in Moratto et al. (2015). This approach has proven effective in computing realistic broadband simulations for horizontal and vertical motion components near the source (Moratto et al., 2015; Parolai et al., 2020; Moratto et al., 2021).

The wave propagation model and the finite fault parameters are the input data needed for simulating the strong ground motion. The source is modelled using the pseudo-dynamic approach (Guatteri et al., 2004;

Mena et al., 2012) to emulate the temporal behaviour of spontaneously propagating dynamic rupture models. Guatteri et al. (2004) demonstrated that the spatial and temporal variations in the slip, rise time and rupture propagation heavily affect the near-source ground motion. Mena et al. (2012) adopted the modified Yoffe function (Tinti et al., 2005) and upgraded the pseudo-dynamic model with a new set of relations that accounts for earthquake size, buried and surface ruptures and includes local rise-time variations and possible super-shear rupture speed. To increase the accuracy in shaping the asperities and the rise time of the sub-faults outside the asperities, we implemented a weighted distribution computed by the slip distribution normalized to the maximum slip of the rupture area.

To validate the correct application of the pseudo-dynamic model in our approach, we computed the source parameters and compared our values with those obtained by the waveform inversions of two earthquakes: the 2008 Iwate-Miyagi (Cultrera et al., 2013) earthquake and the 2009 L'Aquila event (Cirella et al., 2012), whose source parameter distributions were available in the SRCMOD database (Mai and Thingbaijam, 2014). For the 2008 Iwate-Miyagi event, our computed rise time has a median difference of -0.05 from the inversion one; the differences of the peak of the slip-velocity in the source time function ( $V_{\text{peaks}}$ ) have a median of -0.20. In the case of the L'Aquila earthquake, we obtain more significant differences (median of 0.14) with respect to the inversion results of Cirella et al. (2012), probably because of the heterogeneity in the velocity model; the differences in  $V_{\text{peaks}}$  values also have a median of 0.14. In both cases, the rupture time distribution reproduces satisfactorily the results retrieved from the rupture inversions.

## 3.2 The Campotosto scenario input parameters

The selection of the finite fault input parameters for the DSHA at Campotosto is driven by considering the worst scenario case (Kramer 1996) that, in our case, is provided by the probabilistic disaggregation analysis and geological evidence. The DISS database (DISS Working Group, 2018) reports the Campotosto fault as the composite normal seismogenic source of Colfiorito-Campotosto ( $M_{\text{max}}=6.5$ ); further, DISS (2018) and the ITHACA (2019) database report a debated seismogenic source of Mt. Laga based on geological evidence (Blumetti et al., 1993) and associated with an  $M_{\text{max}}=6.6$ , a striking angle of  $150^\circ$  and a steep dip. Boncio et al. (2004) linked the Mt. Laga system to the more detailed Mt. Gorzano fault, considered an active WSW dipping normal fault; in particular, the field observations map the Mt. Gorzano structure as a continuous fault surface 28 km long. In some stretches, the fault scarp is visible and well exposed in the central part of the structure; it strikes  $N140-150^\circ$  and dips  $60-70^\circ$  to the SW. Boncio et al. (2004) estimated an  $M_{\text{max}}=6.7$  for this fault. The same magnitude was assumed by Pace et al. (2006) in designing the seismogenic boxes to compute seismic hazard.

Therefore, we model a 28 km long and 13 km wide rupture area capable of generating an  $M_W$  6.7 ( $M_0 = 1.26 \cdot 10^{19}$  N\*m) earthquake (Fig. 6). The average stress drop is 2.8 MPa, in agreement with the reference values for the studied area (e.g., Rovelli and Calderoni, 2014). The fault strikes  $N150^\circ$  and dips  $65^\circ$  to the SW (Fig. 6) in agreement with ITHACA (2019) and Boncio et al. (2004); the top of the rupture area is fixed at a depth of 1 km, while the simulated earthquakes nucleate at 11–12 km and propagate toward the

surface. The slip distribution is a random field (Mai and Beroza, 2002) stochastically consistent with slip distributions of past earthquakes. We generate five different slip distributions with seven different nucleations placed at the bottom of the fault from NW to SE edge (Fig. 6) to simulate unilateral and bilateral rupture, resulting in 35 input source models (see the electronic supplement Fig. ES3). Our source models encompass the variability observed on the maximum slip (280–450 cm) within the predicted range Thingbaijam and Mai (2016). Such variance in the maximum slip leads to the generation of different asperities and rupture areas, producing variability in the effective stress drop. In contrast, the static stress drop remains constant, being fixed by  $M_W$  and the entire fault area.

The crustal wave velocity model employed for the deterministic computation is taken from Poiata et al. (2012). Malagnini et al. (2011) parameters are used for the stochastic simulations of the high-frequency wave propagation in Central Italy. We do not include site effects in the time series computation.

### 3.3 Validation of the input parameters

To validate the source parametrization and the propagation parameters to be used for the Campotosto scenario, we compute the near-source synthetic seismograms for three moderate earthquakes that occurred in the study area on 2017 January 18, and we compare them with the corresponding records downloaded from the ESM - Engineering Strong-Motion database (Luzi et al., 2016). In particular, the events were recorded in the near-source by the Italian Accelerometric Network - RAN (Zambonelli et al., 2012) stations Poggio Cancelli (PCB) and Sella Pedicate (SPD). The finite fault parameters used in the simulations are taken from Vicic et al. (2020) and listed in Table 1.

Table 1

Finite-fault source parameters were retrieved from Vicic et al. (2020) of the three 2017, January 18 earthquakes occurred in the Campotosto area.

Time	Mw	Lon. (°)/Lat (°) /Dep(km)	Strike/Dip//Rake (degrees)	Len/Wid (km)	Max slip (cm)
09:25:40	5.2	13.277/42.545/10	150/30/-88	6.0/4.0	27
10:14:09	5.6	13.284/42.531/8	161/41/-69	6.5/6.0	48
13:33:36	5.1	13.275/42.473/9.5	190/31/-43	4.0/3.0	21

We show the computed accelerogram and compare the recorded signals in Fig. 7 and the electronic supplement ES4, and ES5. We reproduce the recorded low-frequency displacement satisfactorily at PCB and SPD in amplitude and phase for the three events (Fig. 7a, and in the electronic supplement ES4a, ES5a). Some differences observed at the high frequency of the horizontal component amplitude spectra of PCB (see the electronic supplement Fig. ES5b), placed in the centre of the filling valley (Antonielli et al., 2021), can be due to site effects, as shown by the horizontal to vertical spectral ratio available from the ESM database (Luzi et al., 2016). Other minor discrepancies can be related to unmodelled local propagation effects (e.g. topographic and valley edges).

Finally, the accelerograms obtained from the combination of deterministic and stochastic simulations reproduce all the components of the recorded signals (Fig. 7c, and in the electronic supplement ES4c, ES5c).

## 3.4 Campotosto scenario

We compute the scenario for an  $M_W=6.7$  earthquake in the Campotosto area at PCB and SPD located above the rupture area and to Rio Fucino (RFC), another station belonging to the RAN network, which is very close to the rupture area (Fig. 6); these three sites represent three dams, which confine the Campotosto artificial water reservoir. The peak ground motions (PGMs) mean values obtained using the 35 source models are reported in Table 2. The results are given for each motion component of the receivers (see the electronic supplement Fig. ES6). We also provide the geometrical mean of the horizontal components.

The computed PGA, within the related standard deviation, are compatible with Akkar et al. (2014a, b); the PGV (Peak Ground Velocity) values are more significant than GMM by Akkar et al. (2014a), also considering one standard deviation and the vertical value at RFC and PCB are larger than horizontal ones.

Table 2

PGM and SO were estimated from seismograms simulated for the three considered receivers and from GMM for PGA and PGV (Akkar et al. (2014a, b) for PGD (Goldberg et al. (2021) and for SO Kamai et al. (2014). The horizontal component is computed as the geometrical mean.

PGM	Component	PCB	RFC	SPD	GMM
PGA (cm/s <sup>2</sup> )	East	766 (420–1392)	1041 (672–1612)	504 (222–780)	
	North	724 (371–1497)	691 (446–1069)	474 (222–1013)	
	Vertical	645 (363–1147)	419 (270–649)	500 (275–910)	266 (131–543)
	Horizontal	744 (409–1354)	848 (520–1284)	488 (281–808)	415 (203–845)
PGV (cm/s)	East	66 (40–109)	73 (49–108)	51 (33–79)	
	North	77 (42–140)	55 (34–89)	58 (29–116)	
	Vertical	96 (60–150)	40 (27–59)	75 (46–122)	14 (7–28)
	Hor.	71 (42–117)	64 (42–97)	54 (33–90)	25 (12–50)
PGD (cm)	East	27 (16–45)	19 (13–27)	20 (14–29)	
	North	51 (33–76)	22 (11–43)	39 (24–63)	
	Vertical	99 (68–143)	14 (9–22)	71 (51–98)	
	Horizontal	37 (25–55)	20 (13–32)	28 (19–41)	38 (21–69)
SO (cm)	East	12 (6–24)	5 (2–10)	4 (1–12)	
	North	31 (15–61)	8 (3–17)	17 (8–34)	
	Vertical	-74 (-30-120)	1 (0.2-6)	-40 (-03-62)	PCB: 60 (16–228) SPD: 40 (11–152)
	Horizontal	14 (7–30)	5 (2–10)	9 (5–15)	PCB: 28 (7-106) SPD: 22 (6–83)

The horizontal PGA and PGV values computed for the three receivers (Table 2) are comparable with the strong motion recorded during the 2016 Central Italy sequence when PGA reached 0.87 g while PGV exceeded 80 cm/s at some near-source stations (Suzuki and Iervolino, 2017). Pitarka et al. (2021) simulated ground motion for the 2016 Norcia earthquake, with PGV reaching values of up to 200 cm/s close to a large slip patch. On average, the most considerable shaking is estimated at PCB, located above the rupture area and strongly influenced by near-source effects (Fig. 6). The simulated vertical ground

motion is comparable to the shaking recorded at the near-source station located in Castelluccio di Norcia (CLO) during the  $M_W=6.6$  2016 Norcia earthquake (D'Amico et al., 2019); similarly to PCB, CLO was situated above the rupture area of a strong distensive earthquake.

The horizontal Peak Ground Displacement (PGD) values are consistent with the GMM prediction by Goldberg et al. (2021); the vertical PGD at PCB and SPD is higher than the horizontal values.

The Static Offset (SO) is negligible at RFC, located at the border of the rupture area, whilst it is relevant in the vertical components of PCB and SPD. However, the values are comparable with those obtained by the empirical relation of Kamai et al. (2014). The SO and the vertical response spectra simulated at PCB are also similar to those computed at CLO for the 2016 Norcia earthquake (D'Amico et al., 2019).

The horizontal SA are generally comparable with Akkar et al. (2014a) within the standard deviation (Fig. 8a, 8c, 8e). In comparison, the values of the vertical component (Fig. 8b, 8d, 8f) are higher than Akkar et al. (2014b) for all the receivers. To compare the simulated spectra with recorded ones, we retrieved the spectra of the 2016  $M_W=6.6$  Norcia earthquake (stations CLO and T1214) and the 2016  $M_W=7.0$  Kumamoto earthquake (stations KMM10 and KMM16) from the Ness2.0 database (Sgobba et al., 2021) at stations above the rupture area. In addition to a similar magnitude, these earthquakes were selected for their focal mechanism and vertical  $SO < -40$  cm. Considering the standard deviations, our results are larger than recorded vertical spectra at periods of 0.8 s at PCB and SPD, stations located above the rupture area and strongly influenced by single asperities in the slip distributions and heterogeneities in rise-time and rupture velocity distributions within the source models. The simulated horizontal displacement spectra (SD) are generally consistent with the values estimated by GMM (Cauzzi et al., 2015) within the standard deviation and with the recorded spectra (Fig. 9); the difference observed at  $2.0 < T < 6.0$  s is due to the position of the source that is shallow and close to the receivers. Also, the SD simulated on the mean vertical component is comparable with the recorded spectra in the whole period range.

## 4. Discussion

The PSHA ground motion estimated for the study area can be extracted from the hazard curves for a few return periods. The Italian seismic hazard map (Meletti et al., 2006; Stucchi et al., 2011) defines a PGA of 0.260 and 0.448 g expected at return periods of 475 and 2475 years, respectively; more recent studies estimated higher values of PGA due to the different GMM used. Our PGA values (0.414 and 0.816 g, respectively) result more comparable with these recent studies, although the complete logic tree is very different. The similarity of the results is probably linked to the choice of GMM, despite a completely different approach to seismological sources. Furthermore, our values are comparable with the strong motion recorded during the 2016 Central Italy sequence when PGA reached 0.87 g.

In general, the worst-case DSHA scenario ground shaking is comparable with the empirical GMM estimations within one standard deviation. The variability of input source parameters like  $M_W$ , rupture

area and the focal mechanism is limited by the a priori PSHA assumptions; however, these limitations are reliable constraints for our results. Central Italy is a well monitored and studied area with known tectonic settings and quite good knowledge of various seismogenic sources (see sections 1 and 3.2 for references).

The simulated shaking is very sensitive to source parameters such as spatial heterogeneity of slip, rise time and rupture velocity on the fault volume; the seismic moment distributions and asperities patches can generate very high strong motion in near-source, particularly on the longer periods and with significantly associated uncertainties (Moratto et al., 2017; Causse et al., 2021; Pischiutta et al., 2021; Pitarka et al., 2021). For these reasons, the scenario generated utilizing 35 rupture models evidences a substantial variability; the standard deviations associated with the mean values are larger than those related to GMM, and they can exceed 50% of the mean values. In particular, the variability is more considerable for periods lower than 0.5 s, agreeing with Valentova et al. (2021), who observed that the between-event variability increases at periods < 1 s. This trend is steeper in the near-source region and can reach the within-event variability value. The highest values are generated by the bilateral ruptures associated with the seismic moment distributions and the largest slip in our scenario. The shaking computed at various receivers is also influenced by the source approximation, the distance and the directivity effects of the rupture propagation; the updip propagation generates strong directivity effects around the surface exposure or its up-dip projection (Somerville 2003). In our scenario, the rupture area is modelled as a planar fault, but some authors (Valoroso et al., 2013; Vicic et al., 2020) suggest a listric fault; the simplification of the fault geometry could increase PGV values on the hanging wall and a decrement on the footwall (Passone and Mai, 2017). The amplitude ratio between the three motion components is also linked to different radiation patterns generated by various source models. Therefore a translation of the fault plane with respect to the original model could generate results different from those computed in this study.

The increase of the recording stations and the available seismograms evidences the relevance of the vertical motion for the shaking observed in the near-source (e.g., Di Sarno et al., 2010; Suzuki and Iervolino, 2017; D'Amico et al., 2019); at the same time, the development of the computation models allow to simulate accurately these effects giving a good agreement between the theoretical models and the observations.

In our scenario, the most significant shaking values in the vertical component are observed at longer periods for receivers located above the fault (PCB and SPD). In this case, the normal-type source generates a strong subsidence effect. The ratio between the vertical and horizontal ground acceleration peak exceeds the unity in many other cases (e.g., Elgamal and He, 2004; Shrestha, 2009; Kim et al., 2011).

The validation process is fundamental to obtaining a reliable estimation of the seismic hazard and to assessing the seismic safety of large structures (e.g., dams), which may be strongly influenced by spatial variability in one or both the horizontal directions of the input motion (Dello Russo et al., 2017). Grimaz

and Malisan (2014) evidenced a deficiency of seismic safety in the near-source if the design does not consider the seismic effects.

## 5. Conclusions

Reliable estimates of the ground motion in the near-source are crucial to evaluating the seismic hazard, mainly if some critical facilities operate there. Ground motion models are weakly constrained in the near source because of the lack of recorded waveforms. Numerical simulations can fill the gap and provide the input design for specific sites.

We apply the PSHA and the DSHA to estimate the near-source seismic hazard for three dams closing the water impoundment in the Campotosto area (Central Italy). The PSHA is performed following the approach of seismotectonic probabilism by modelling fault sources. The disaggregation of the probabilistic seismic hazard, calculated for the return period of 2475 years, provides the magnitude-distance pair of  $M_w=6.75 \pm 0.25$  within the first 10 km of distance. This magnitude-distance pair represents the most influencing earthquake for the hazard estimate in the study area. The DSHA assumes as the worst possible case an  $M_w = 6.7$  earthquake, consistently with some field geology studies (e.g., Boncio et al., 2004) and provides the ground motion for three receivers at the three dams.

We reproduce the variability due to the source rupture parameters that affects the simulated ground motion and that are not reproduced by the GMM in the near-source. This variability is related to the rupture propagation model heterogeneities and reliable finite fault parameters input in the modelling. The most significant ground motion values are obtained above the rupture area, at the receiver PCB, particularly at long periods. At the same time, high-frequency shaking characterizes the receiver RFC, placed at the edge of the main fault. On average, the associated variability can reproduce the strong motion characteristics recorded in near-source for similar earthquakes.

The Campotosto scenario shows that the vertical component might experience shaking values comparable with the horizontal, and, therefore, it cannot be ignored in near-source studies. Our vertical peak parameters and spectra are consistent with the values recorded for the Norcia 2016 mainshock, and the observed low frequency contribute (PGD and SO). GMM probably underestimates the vertical component's ground motion, especially at longer periods and above the rupture area. Numerical simulations can exceed the limits of the GMM in the near source to fit observations and define reliable seismic input. However, ground motion simulations require a constrained definition for the seismic source, the propagation and local site effects; adequate knowledge of these parameters' bounds is a primary key to defining reliable, strong motion and uncertainties of the results.

## Declarations

**Acknowledgements** We thank Seyyedmaalek Momeni, who provided us with the slip distribution for the earthquakes that occurred on January 18, 2017, and Laura Peruzza for her valuable suggestions on fault

PSHA.

**Competing Interests** The authors have no relevant financial or non-financial interests to disclose.

**Funding** The authors declare that no funds, grants, or other support were received during the preparation of this manuscript.

## References

1. Akkar S, Sandikkaya MA, Bommer JJ (2014a) Empirical ground-motion models for point- and extended-source crustal earthquake scenarios in Europe and the Middle East. *Bull Earthq Eng* 12:359–387. <https://doi.org/10.1007/s10518-013-9461-4>
2. Akkar S, Sandikkaya MA, Ay BO (2014b) Compatible ground-motion prediction equations for damping scaling factors and vertical-to-horizontal spectral amplitude ratios for the broader Europe region. *Bull Earthq Eng* 12:517–547. <https://doi.org/10.1007/s10518-013-9537-1>
3. Antonielli B, Bozzano F, Fiorucci M, Hailemichael S, Iannucci R, Martino S, Rivellino S, Scarascia Mugnozza G (2021) Engineering-geological features supporting a seismic-driven multi-hazard scenario in the Lake Campotosto Area (L'Aquila, Italy). *Geosciences* 11:107. <https://doi.org/10.3390/geosciences11030107>
4. Barani S, Scafidi D, Eva C (2010) Strain rates in northwestern Italy from spatially smoothed seismicity. *J Geoph Res* 115:B07302. <https://doi.org/10.1029/2009JB006637>
5. Bindi D, Pacor F, Luzi L, Puglia R, Massa M, Ameri G, Paolucci R (2011) Ground motion prediction equations derived from the Italian strong motion database. *Bull Earthq Eng* 9:1899–1920. <https://doi.org/10.1007/s10518-011-9313-z>
6. Bindi D, Massa M, Luzi L, Ameri G, Pacor F, Puglia R, Augliera P (2014) Pan-European ground motion prediction equations for the average horizontal component of PGA, PGV and 5%-damped PSA at spectral periods of up to 3.0 s using the RESORCE dataset. *Bull Earthq Eng* 12:391 – 340. <https://doi.org/10.1007/s10518-013-9525-5>
7. Blumetti AM, Dramis F, Michetti AM (1993) Fault-generated mountain fronts in the Central Apennines (Central Italy): geomorphological features and seismotectonic implications. *Earth Surf Proc Land* 18:203–223. <https://doi.org/10.1002/esp.3290180304>
8. Bommer JJ (2002) Deterministic vs probabilistic seismic hazard assessment: an exaggerated and obstructive dichotomy. *J Earthq Eng* 6:43–73. <https://doi.org/10.1080/13632460209350432>
9. Boncio P, Lavecchia G, Milana G, Rozzi B (2004) Seismogenesis in central Apennines, Italy: an integrated analysis of minor earthquake sequences and structural data in the Amatrice-Campotosto area. *Ann Geophys* 47:1723–1742. <https://doi.org/10.4401/ag-3371>
10. Boore DM (2009) Comparing stochastic point-source and finite-source ground motion simulations: SMSIM and EXSIM. *Bull Seismol Soc Am* 99:3202–3216. <https://doi.org/10.1785/0120090056>

11. Causse M, Cornou C, Maufroy E, Grasso JR, Baillet L, El Haber E (2021) Exceptional ground motion during the shallow Mw 4.9 2019 Le Teil earthquake, France. *Commun Earth Environ* 2:14. <https://doi.org/10.1038/s43247-020-00089-0>
12. Cauzzi C, Faccioli E, Vanini M, Bianchini A (2015) Updated predictive equations for broadband (0.01–10 s) horizontal response spectra and peak ground motions, based on a global dataset of digital acceleration records. *Bull Earthq Eng* 13:1587–1612. <https://doi.org/10.1007/s10518-014-9685-y>
13. Chartier T, Scotti O, Lyon-Caen H (2019) SHERIFS: open-source code for computing earthquake rates in fault systems and constructing hazard models. *Seismol Res Lett* 90:1678–1688. <https://doi.org/10.1785/0220180332>
14. Chiarabba C, Amato A, Anselmi M, Baccheschi P, Bianchi I, Cattaneo M, Cecere G, Chiaraluce L, Ciaccio MG, De Gori P, De Luca G, Di Bona M, Di Stefano R, Faenza L, Govoni A, Improta L, Lucente FP, Marchetti A, Margheriti L, Mele F, Michelini A, Monachesi G, Moretti M, Pastori M, Piana Agostinetti N, Piccinini D, Roselli P, Seccia D, Valoroso L (2009) The 2009 L'Aquila (central Italy)  $M_w$ 6.3 earthquake: Main shock and aftershocks. *Geophys Res Lett* 36:L18308. <https://doi.org/10.1029/2009GL039627>
15. Chiaraluce L, Di Stefano R, Tinti E, Scognamiglio L, Michele M, Casarotti E, Cattaneo M, De Gori P, Chiarabba C, Monachesi G, Lombardi A, Valoroso L, Latorre D, Marzorati S (2017) The 2016 Central Italy seismic sequence: A first look at the mainshock, aftershocks, and source models. *Seism Res Lett* 88:757–771. <https://doi.org/10.1785/0220160221>
16. Cirella A, Piatanesi A, Tinti E, M. Chini, Cocco M (2012) The complexity of the rupture process during the 2009 L'Aquila, Italy, earthquake. *Geophys J Int* 190:607–621. <https://doi.org/10.1111/j.1365-246X.2012.05505.x>
17. Cornell CA (1968) Engineering seismic risk analysis. *Bull Seism Soc Am* 54:1583-1606.
18. Cultrera G, Ameri G, Saraò A, Cirella A, Emolo A (2013) Ground-motion simulations within ShakeMap methodology: Application to the 2008 Iwate–Miyagi Nairiku (Japan) and 1980 Irpinia (Italy) earthquakes. *Geophys J Int* 193:220–237. <https://doi.org/10.1093/gji/ggs074>
19. D'Amico M, Felicetta C, Schiappapietra E, Pacor F, Gallovic F, Paolucci R, Puglia R, Lanzano G, Sgobba S, Luzi L (2019) Fling effects from near-source strong-motion records: insights from the 2016 Mw 6.5 Norcia, Central Italy, earthquake. *Seismol Res Lett* 90:659–671. <https://doi.org/10.1785/0220180169>
20. Dello Russo A, Sica S, Del Gaudio S, De Matteis R, Zollo A (2017) Near-source effects on the ground motion occurred at the Conza Dam site (Italy) during the 1980 Irpinia earthquake. *Bull Earthq Eng* 15:4009–4037. <https://doi.org/10.1007/s10518-017-0138-2>
21. Di Sarno L, Elnashai AS, Manfredi G (2010) Seismic response of R.C. members subjected to the 2009 L'Aquila (Italy) near-field earthquake ground motions. Report No.01-2010. Mid-America Earthquake Center, University of Illinois at Urbana-Champaign, USA.
22. DISS Working Group (2018) Database of Individual Seismogenic Sources (DISS), Version 3.2.1: A compilation of potential sources for earthquakes larger than M 5.5 in Italy and surrounding areas.

<http://diss.rm.ingv.it/diss/>, Istituto Nazionale di Geofisica e Vulcanologia.

<https://doi.org/10.6092/INGV.IT-DISS3.2.1>

23. Elgamal A, He LC (2004) Vertical earthquake ground motion records: An overview. *J Earthq Eng* 8:663–697. <https://doi.org/10.1080/13632460409350505>
24. Faure Walker JP, Boncio P, Pace B, Roberts GP, Benedetti L, Scotti O, Visini F, Peruzza L (2020) Fault2SHA Central Apennines Database. Institute for Risk and Disaster Reduction. University College London, PANGAEA. <https://doi.org/10.1038/s41597-021-00868-0>
25. Falcucci E, Gori S, Bignami C, Pietrantonio G, Melini D, Moro M, Saroli M, Galadini F (2018) The Campotosto Seismic gap in between the 2009 and 2016–2017 seismic sequences of central Italy and the role of inherited lithospheric faults in regional seismotectonic settings. *Tectonics* 37:2425–2445. <https://doi.org/10.1029/2017TC004844>
26. Galadini F, Galli P (2003) Paleoseismology of silent faults in the Central Apennines (Italy): The Mt. Vettore and Laga Mts. Faults. *Ann Geophys* 46:815–836. <https://doi.org/10.4401/ag-3457>
27. Grimaz S, Malisan P (2014) Near field domain effects and their consideration in the international and Italian seismic codes. *Boll Geof Teor Appl* 55:717–738. <https://doi.org/10.4430/bgta0130>
28. Goldberg DE, Melgar D, Hayes GP, Crowell BW, Sahakian VJ (2021) A Ground-Motion Model for GNSS Peak Ground Displacement. *Bull Seismol Soc Am* 111:2393–2407. <https://doi.org/10.1785/0120210042>
29. Guatteri M, Mai PM, Beroza GC (2004) A pseudo-dynamic approximation to dynamic rupture models for strong ground motion prediction. *Bull Seismol Soc Am* 94:2051–2063. <https://doi.org/10.1785/0120040037>
30. Gutenberg R, Richter CF (1944) Frequency of earthquakes in California. *Bull Seismol Soc Am* 34:185–188.
31. ITHACA Working Group (2019) ITHACA (ITaly HAZard from CApable faulting), A database of active capable faults of the Italian territory. Version December 2019. ISPRA Geological Survey of Italy. Web Portal <http://sgi2.isprambiente.it/ithacaweb/Mappatura.aspx>
32. Kamai R, Abrahamson N, Gaves R (2014) Adding fling effects to processed ground-motion time histories. *Bull Seismol Soc Am* 104:1914–1929. <https://doi.org/10.1785/0120130272>
33. Kim SJ, Holub CJ, Elnashai AS (2011) Analytical assessment of the effect of vertical earthquake motion on R.C. bridge piers. *J Struct Eng* 137:252–260.
34. Kramer SL (1996) *Geotechnical Earthquake Engineering*. Prentice Hall Inc., New Jersey, 114–115.
35. Krinitzsky EL (2003) How to combine deterministic and probabilistic methods for assessing earthquake hazards. *Eng Geol* 70:157–163. [https://doi.org/10.1016/S0013-7952\(02\)00269-7](https://doi.org/10.1016/S0013-7952(02)00269-7)
36. Leonard M (2010) Earthquake fault scaling: Self-consistent relating of rupture length, width, average displacement, and moment release. *Bull Seismol Soc Am* 100:1971–1988. <https://doi.org/10.1785/0120090189>

37. Luzi L, Puglia R, Russo E & ORFEUS WG5 (2016) Engineering Strong Motion Database, version 1.0. Istituto Nazionale di Geofisica e Vulcanologia, Observatories & Research Facilities for European Seismology. <https://doi.org/0.13127/ESM>
38. Mai PM (2009) Ground motion: Complexity and scaling in the near field of earthquake ruptures, in *Encyclopedia of Complexity and Systems Science*, W.H.K. Lee and R. Meyers (Editors), Springer, New York, 4435–4474.
39. Mai PM, Beroza GC (2002) A spatial random-field model to characterize complexity in earthquake slip. *J Geophys Res* 107:2308. <https://doi.org/10.1029/2001JB000588>
40. Mai PM, Thingbaijam KKS (2014) SRCMOD: An online database of finite-fault rupture models. *Seism Res Lett* 85:1348–1357. <https://doi.org/10.1785/0220140077>
41. Malagnini L, Akinci A, Mayeda K, Munafo I, Herrmann RB, Mercuri A (2011) Characterization of earthquake-induced ground motion from the L'Aquila seismic sequence of 2009, Italy. *Geophys J Int* 184:325–337. <https://doi.org/0.1111/j.1365-246X.2010.04837.x>
42. Martelli L, Santulin M, Sani F, Tamaro A, Bonini M, Rebez A, Corti G, Slejko D (2017) Seismic hazard of the Northern Apennines based on 3D seismic sources. *J Seismol* 21:1251–75. <https://doi.org/10.1007/s10950-017-9665-1>
43. McGuire RK (1995) Probabilistic seismic hazard analysis and design earthquakes: Closing the loop. *Bull Seismol Soc Am* 85:1275–1284.
44. McGuire RK (2001). Deterministic vs. probabilistic earthquake hazard and risks. *Soil Dyn Earthq Eng* 21:377–384. [https://doi.org/10.1016/S0267-7261\(01\)00019-7](https://doi.org/10.1016/S0267-7261(01)00019-7)
45. Meletti C, Montaldo V, Stucchi M, Martinelli F (2006) Database della pericolosità sismica MPS04. Istituto Nazionale di Geofisica e Vulcanologia (INGV). <https://doi.org/10.13127/SH/MPS04/DB>
46. Meletti C, D'Amico V, Martinelli F, Rovida A (2019) Prodotto 2.15: stima delle completezze di CPT15 e suo declustering. In: *Il modello di pericolosità sismica MPS19. Final Report*. Editors C. Meletti and W. Marzocchi (Roma: CPS-INGV), 168.
47. Mena B, Dalguer LA, Mai PM (2012) Pseudodynamic source characterization for strike-slip faulting including stress heterogeneity and super-shear ruptures. *Bull Seismol Soc Am* 102:1654–1680. <https://doi.org/10.1785/0120110111>
48. Moratto L, Vuan A, Saraò A (2015) A Hybrid Approach for Broadband Simulations of Strong Ground Motion: The Case of the 2008 Iwate–Miyagi Nairiku Earthquake. *Bull Seismol Soc Am* 105:2823–2829. <https://doi.org/10.1785/0120150054>
49. Moratto L, Saraò A, Vuan A, Mucciarelli M, Jimenez M, Garcia Fernandez M (2017) The 2011  $M_w$  5.2 Lorca earthquake as a case study to investigate the ground motion variability related to the source model. *Bull Earthq Eng* 15:3463–3482. <https://doi.org/10.1007/s10518-017-0110-1>
50. Moratto L, Vuan A, Saraò A, Slejko D, Papazachos C, Caputo R, Civile D, Volpi V, Ceramicola S, Chatzipetros A, Daja S, Fabris P, Garcia-Pelaez J, Geletti R, Karvelis P, Pavlides S, Rapti D, Rebez A, Rossi G, Sandron D, Santulin M, Sboras S, Tamaro A, Zecchin M, Zgur F, Zuliani D (2021) Seismic

- Hazard for the Trans Adriatic Pipeline (TAP). Part 2: Broadband scenarios at Fier compressor station (Albania). *Bull Earthq Eng* 19:3389–3413. <https://doi.org/10.1007/s10518-021-01122-z>
51. Motazedian D, Atkinson GM (2005) Stochastic finite-fault modeling based on a dynamic corner frequency. *Bull Seismol Soc Am* 95:995–1010. <https://doi.org/10.1785/0120030207>
  52. Pace B, Peruzza L, Lavecchia G, Boncio P (2006) Layered seismogenic source model and probabilistic seismic hazard analyses in Central Italy. *Bull Seismol Soc Am* 96:107–132. <https://doi.org/10.1785/0120040231>
  53. Pagani M, Monelli D, Weatherill G, Danciu L, Crowley H, Silva V, Henshaw P, Butler L, Nastasi M, Panzeri L, Simionato M (2014) OpenQuake engine: An open hazard (and risk) software for the global earthquake model. *Seismol Res Lett* 85:692–702. <https://doi.org/10.1785/0220130087>
  54. Parolai S, Moratto L, Bertoni M, Scaini C, Rebez A (2020) Could a decentralized onsite earthquake early warning system help in mitigating seismic risk in North-eastern Italy? The case of the Ms 6.5 1976 Friuli earthquake. *Seismol Res Lett* 91:3323–3333. <https://doi.org/10.1785/0220200177>
  55. Passone L, Mai PM (2017) Kinematic earthquake ground-motion simulations on listric normal faults. *Bull Seismol Soc Am* 107:2980–2993. <https://doi.org/10.1785/0120170111>
  56. Pischiutta M, Akinci A, Tinti E, Herrero A (2021) Broad-band ground-motion simulation of 2016 Amatrice earthquake, Central Italy. *Geophys J Int* 224:1753–1779. <https://doi.org/10.1093/gji/ggaa412>.
  57. Pitarka A, Akinci A, De Gori P, Buttinelli M (2021) Deterministic 3D ground-motion simulations (0–5 Hz) and surface topography effects of the October 30, 2016, Mw 6.5 Norcia, Italy, earthquake. *Bull Seismol Soc Am* 112:262–286. <https://doi.org/10.1785/0120210133>
  58. Poiata N, Koketsu K, Vuan A, Miyake H (2012) Low-frequency and broad-band source models for the 2009 L'Aquila, Italy, earthquake. *Geophys J Int* 191:224–242. <https://doi.org/10.1111/j.1365-246X.2012.05602.x>
  59. Renault P (2014) Approach and challenges for the seismic hazard assessment of nuclear power plants: the Swiss experience. *Boll Geof Teor Appl* 55:149–164. <https://doi.org/10.4430/bgta0089>
  60. Rovelli A, Calderoni G (2014) Stress drops of the 1997–1998 Colfiorito, Central Italy earthquakes: hints for a common behaviour of normal faults in the Apennines. *Pure and Appl Geophys* 171:2731–2746. <https://doi.org/10.1007/s00024-014-0856-1>
  61. Rovida A, Locati M, Camassi R, Lolli B, Gasperini P (2019) *Catalogo Parametrico dei Terremoti Italiani (CPTI15), versione 2.0*. Italy: Istituto Nazionale di Geofisica e Vulcanologia (INGV).
  62. Rovida A, Locati M, Camassi R, Lolli B, Gasperini P (2020) The Italian earthquake catalogue CPTI15. *Bull Earthq Eng* 18:2953–2984. <https://doi.org/10.1007/s10518-020-00818-y>
  63. Santulin M, Tamaro A, Rebez A, Slejko D, Sani F, Martelli L, Bonini M, Corti G, Poli ME, Zanferrari A, Marchesini A, Busetti M, Dal Cin M, Spallarossa D, Barani S, Scafidi D, Barreca G, Monaco C (2017) Seismogenic zonation as a branch of the logic tree for the new Italian seismic hazard map - MPS16: a preliminary outline. *Boll Geof Teor Appl* 58:313–342.

64. Schiappapietra E, Smerzini C (2021) Spatial correlation of broadband earthquake ground motion in Norcia (Central Italy) from physics-based simulations. *Bull Earthq Eng* 19:4693–4717. <https://doi.org/10.1007/s10518-021-01160-7>
65. Scotti O, Visini F, Faure Walker J, Peruzza L, Pace B, Benedetti L, Boncio P, Roberts G (2021) Which Fault Threatens Me Most? Bridging the Gap Between Geologic Data- Providers and Seismic Risk Practitioners. *Front Earth Sci* 8:626401. <https://doi.org/10.3389/feart.2020.626401>
66. Sgobba S, Felicetta C, Lanzano G, Ramadan F, D'Amico M, Pacor F (2021) NESS2.0: an updated version of the worldwide dataset for calibrating and adjusting ground-motion models in near source. *Bull Seismol Soc Am* 111:2358–2378. <https://doi.org/10.1785/0120210080>
67. Shrestha B (2009) Effects of near field vertical acceleration on seismic response of the long span cable stayed bridge. MSc, Dissertation, Pulchok campus I.O.E., Tribhuvan University.
68. Slejko D, Rebez A, Santulin M, Garcia-Pelaez J, Sandron D, Tamaro A, Caputo R, Ceramicola S, Chatzipetros A, Civile D, Daja S, Fabris P, Geletti R, Karvelis P, Moratto L, Papazachos C, Pavlides S, Rapti D, Rossi G, Saraò A, Sboras S, Volpi V, Vuan A, Zecchin M, Zgur F, Zuliani D (2021) Seismic Hazard for the Trans Adriatic Pipeline (TAP). Part 1: probabilistic seismic hazard analysis along the pipeline. *Bull Earthq Eng* 19:3349–3388. <https://doi.org/10.1007/s10518-021-01111-2>
69. Somerville PG (2003) Magnitude scaling of the near fault rupture directivity pulse. *Phys Earth Planet Inter* 137:201–212.
70. Spudich P, Xu L (2003) Documentation of software package Compsyn svx3.11: programs for earthquake ground motion calculation using complete 1-d green's functions, *International Handbook of Earthquake and Engineering Seismology CD, Int. Ass. Of Seismology and Physics of Earth's Interior*, Academic Press.
71. Spudich P, Rowshandel B, Shahi SK, Baker JK, Chiou BSJ (2014) Overview and comparison of the NGA-West2 directivity models. *Earthquake Spectra* 30:1199–1221. <https://doi.org/10.1193/080313EQS222M>
72. Stucchi M, Meletti C, Montaldo V, Crowley H, Calvi GM, Boschi E (2011). Seismic Hazard Assessment (2003–2009) for the Italian Building Code. *Bull Seismol Soc Am* 101:1885–1911. <https://doi.org/10.1785/0120100130>
73. Suzuki A, Iervolino I (2017) Italian vs worldwide history of largest PGA and PGV. *Ann Geophys* 60:S0551. <https://doi.org/10.4401/ag-7391>
74. Tamaro A, Grimaz S, Santulin M, Slejko D (2018) Characterization of the expected seismic damage for a critical infrastructure: the case of the oil pipeline in Friuli Venezia Giulia (N.E. Italy). *Bull Earthq Eng* 16:1425–1445. <https://doi.org/10.1007/s10518-017-0252-1>
75. Tinti E, Fukuyama E, Piatanesi A, Cocco M (2005) A Kinematic Source-Time Function Compatible with Earthquake Dynamics. *Bull Seismol Soc Am* 95:1211–1223. <https://doi.org/10.1785/0120040177>
76. Tondi E, Jablonská D, Volatili T, Michele M, Mazzoli S, Pierantoni PP (2021) The Campotosto linkage fault zone between the 2009 and 2016 seismic sequences of central Italy: implications for seismic

- hazard analysis. *GSA Bulletin* 133:1679–1694. <https://doi.org/10.1130/B35788.1>
77. Valentová L, Gallovic F, Hok S (2021) Near-source ground motions and their variability derived from dynamic rupture simulations constrained by NGA-West2 GMPEs. *Bull Seismol Soc Am* 111:2559–2573. <https://doi.org/10.1785/0120210073>
  78. Valoroso L, Chiaraluce L, Piccinini D, Di Stefano R, Schaff D, Waldhauser F (2013) Radiography of a normal fault system by 64,000 high-precision earthquake locations: the 2009 L'Aquila (Central Italy) case study. *J Geophys Res Solid Earth* 118:1156–1176. <https://doi.org/10.1002/jgrb.50130>
  79. Vivic B, Aoudia A, Borghi A, Momeni S, Vuan A (2020) Seismic and geodetic transients in Central Apennines from 2008 to 2018. *Geophys Res Lett.* <https://doi.org/10.1002/essoar.10502692.3>
  80. Vuan A, Sugan M, Chiaraluce L, Di Stefano R (2017) Loading rate variations along a midcrustal shear zone preceding the Mw6.0 earthquake of August 24, 2016, in Central Italy. *Geophys Res Lett* 44:12170–12180. <https://doi.org/10.1002/2017GL076223>
  81. Vuan A, Sugan M, Amati G, Kato A (2018) Improving the detection of low-magnitude seismicity preceding the Mw6.3 L'Aquila earthquake: Development of a scalable code based on the cross correlation of template earthquakes. *Bull Seismol Soc Am* 108:471–480. <https://doi.org/10.1785/0120170106>
  82. Xin D, Zhang Z (2021) On the comparison of seismic ground motion simulated by physics-based dynamic rupture and predicted by empirical attenuation equations. *Bull Seismol Soc Am* 111:2595–2616. <https://doi.org/10.1785/0120210077>
  83. Wells DL, Coppersmith KJ (1994) New empirical relationship among magnitude, rupture length, rupture width, rupture area, and surface displacement. *Bull Seismol Soc Am* 84:974–1002.
  84. Woessner J, Danciu L, Giardini D, Crowley H, Cotton F, Grünthal G, Valensise G, Arvidsson R, Basili R, Demircioglu MB, Hiemer S, Meletti C, Musson RW, Rovida AN, Sesetyan K, Stucchi M, The SHARE Consortium (2015) The 2013 European seismic hazard model: Key components and results. *Bull Earthq Eng* 13:3553–3596. <https://doi.org/10.1007/s10518-015-9795-1>
  85. Zambonelli E, De Nardis R, Filippi L, Nicoletti M, Dolce M (2012) Performance of the Italian strong motion network during the 2009, L'Aquila seismic sequence (central Italy). *Bull Earthq Eng* 9:39–65. <https://doi.org/10.1007/s10518-010-9218-2>

## Figures

### Figure 1

Map of the study area with the capable active faults (red lines) taken from the Fault2SHA CAD (Faure Walker et al., 2020); the historical (circles) and major instrumental earthquakes (stars) are also plotted.

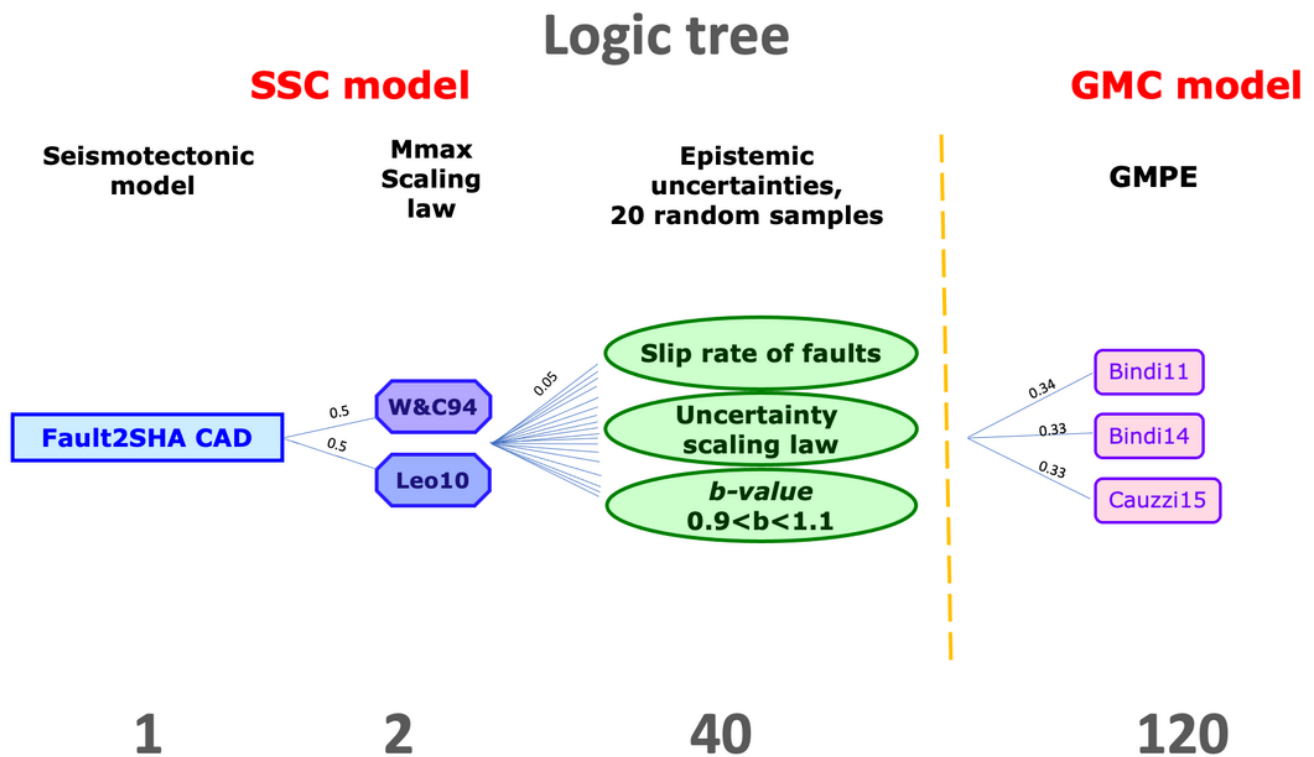


**Figure 2**

The logic tree adopted in our analysis consists of one seismotectonic model (Fault2SHA CAD), two scaling laws for the maximum magnitude definition (W&C94 and Leo10), twenty random samples to explore the epistemic uncertainties of the faults slip rate, the scaling law parameters, and the *b*-value adopted for the target MFD. In addition, the uncertainty about the GMM is explored by including three branches (Bindi11, Bindi14, Cauzzi15). The numbers indicate the branches at each node of the logic tree.

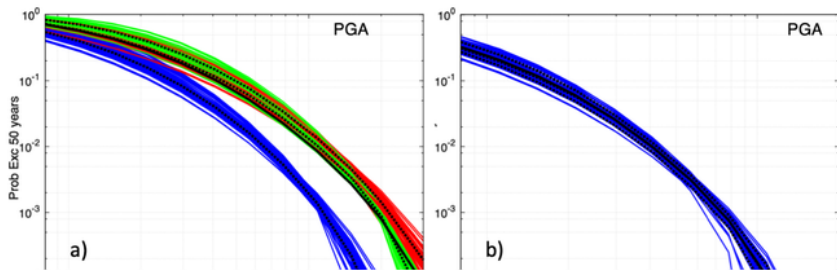


**Figure 3**

PSHA results for the Campotosto site. Hazard curves for (a) horizontal and (b) vertical components; UHRS, for a 2475 year return period, for (c) horizontal and (e) vertical components; UHRS, for a 475 year return period, for (d) horizontal and (f) vertical components. Blue lines for the Bindi et al., 2011, red ones for the Bindi et al., 2014 and green for the Cauzzi et al., 2015. The mean values (continuous lines) and the 16, 50 and 84th percentiles (dotted lines) are in black.

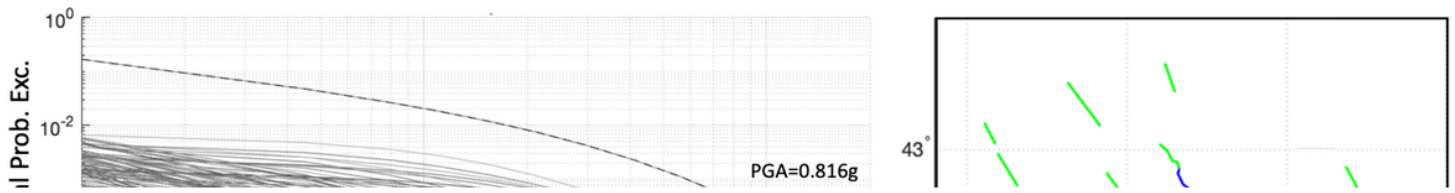


**Figure 4**

PSHA results for Campotosto: a) PGA hazard curves are computed at the Campotosto site for each rupture scenario defined; the sum of all the hazard curves gives the total hazard at the site (dashed line). The black dot represents the PGA value corresponding to a 2475 years return period. b) The slip rates of the sections of the faults involved in the seismic hazard computation.

**Figure 5**

a) The contribution of the sections, for each PGA level, to the probability of exceedance (POE) of that PGA level; the black lines correspond to the 475 and 2475 years return period. b) The PGA map for the 2475 years return period and the sections of the faults that contribute most to the hazard of the Campotosto site (PGA 0.816 g) and surroundings for that return period.

**Figure 6**

The rupture area of the Campotosto fault (green rectangle), the seven nucleations of the rupture (green stars) and the three receivers (yellow triangles) considered in the scenario modelling. The associated

focal mechanism (Boncio et al., 2004) is plotted in the top right inset. We also show the capable active faults (red lines).

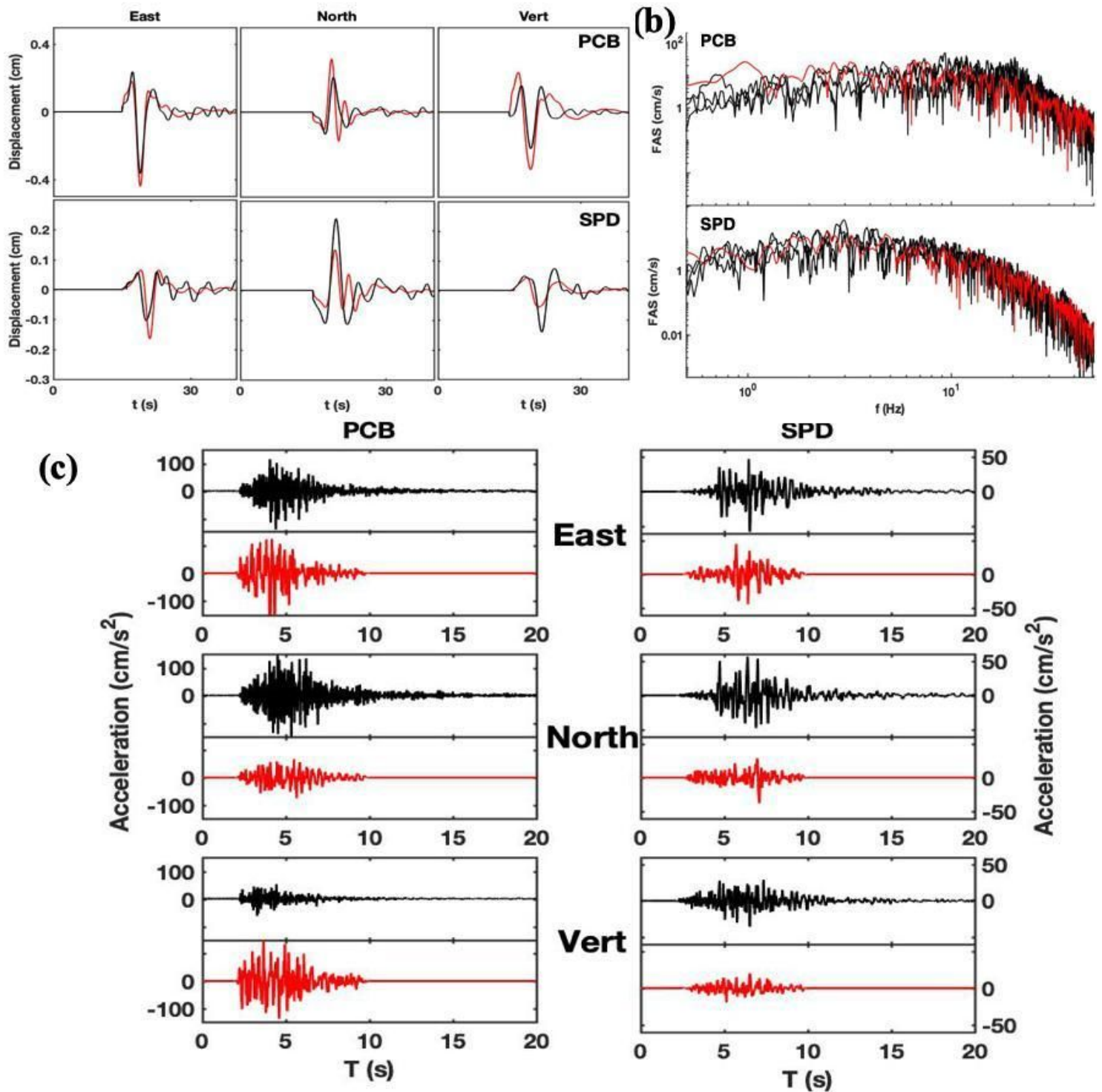


Figure 7

Comparison between recorded (black lines) and simulated waveforms (red lines) for the earthquake ( $M_W=5.2$ ) that occurred on 2017 January 18 at 09:25. (a) Recorded vs deterministic displacement signals

filtered between 0.08 and 0.5 Hz, (b) recorded vs stochastic accelerometric spectra, (c) recorded vs broadband simulated waveforms.

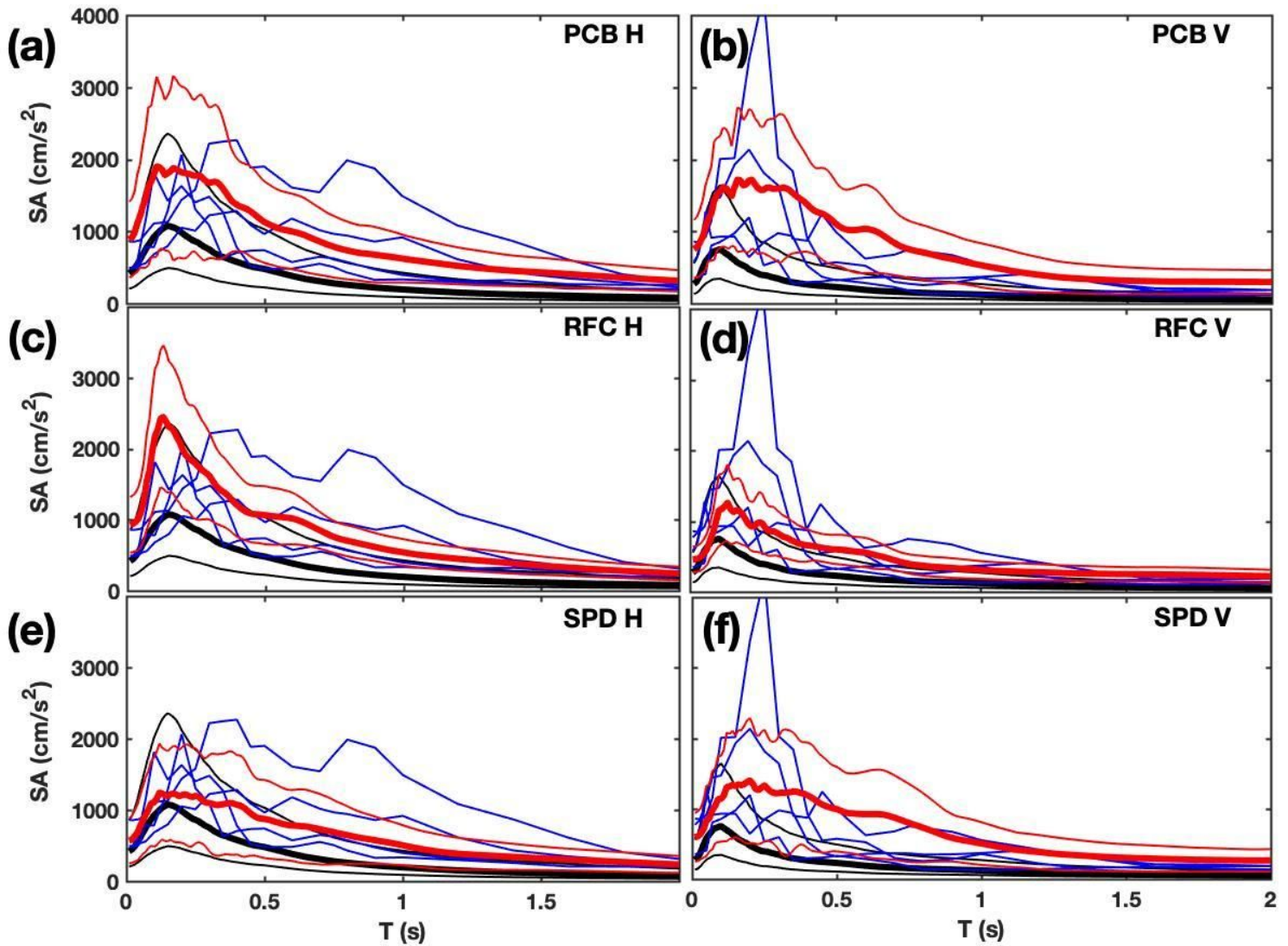


Figure 8

Comparison between GMMs (bold black lines) by Akkar et al. (2014 a, b), recorded SA spectra (blue lines) retrieved from Sgobba et al. (2021), and DSHA mean acceleration spectra (bold red lines) at a) and b) PCB, c) and d) RFC; e) and f) SPD; on the left panels the horizontal component (geometrical mean), on the right boards the vertical component. The thin red and black lines show the related standard deviation.

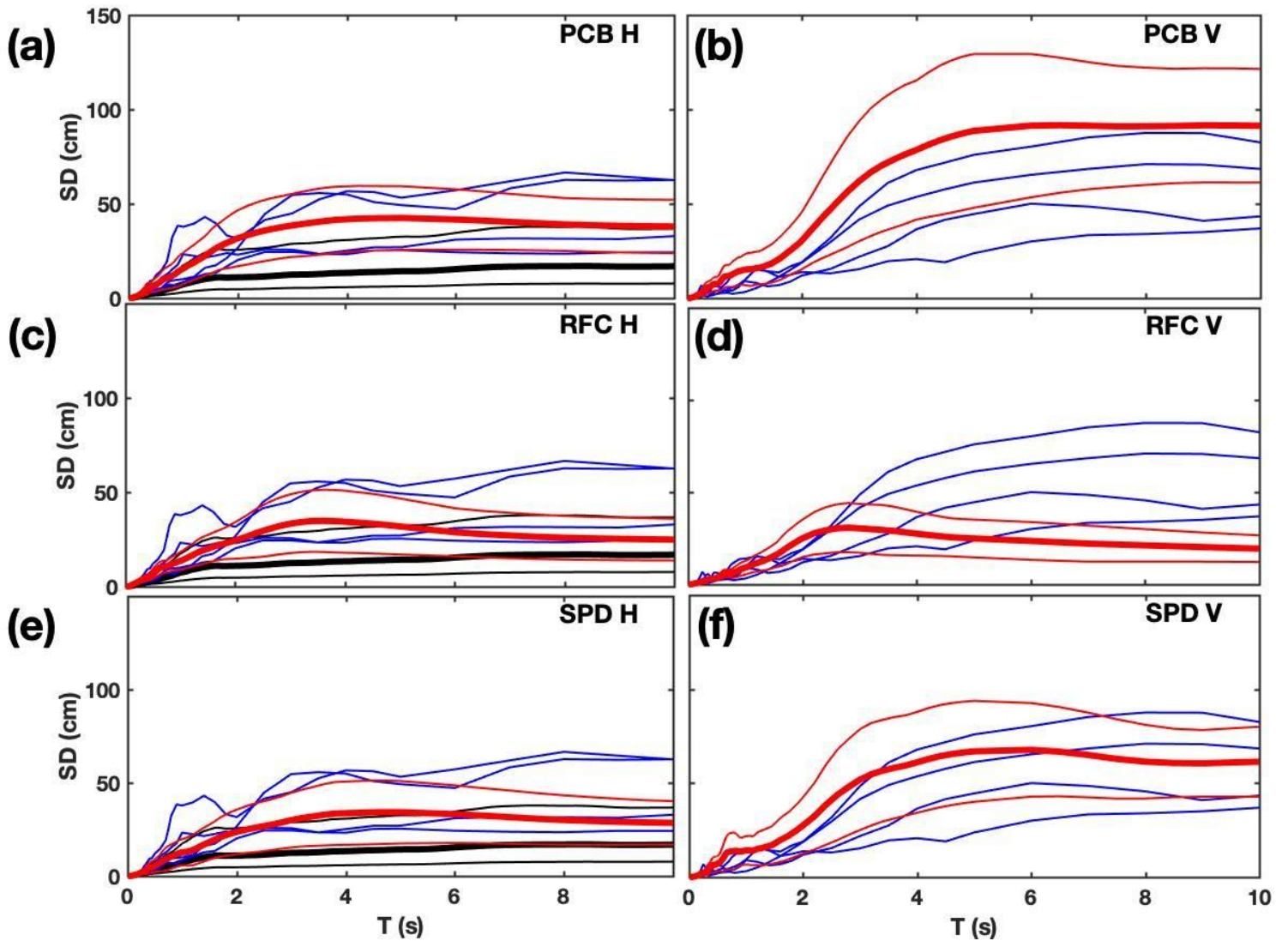


Figure 9

Comparison between GMM (Cauzzi et al., 2015; black lines), recorded SD spectra (Sgobba et al., 2021; blue lines), and DSHA mean displacement spectra (red lines) at a) and b) PCB, c) and d) RFC; e) and f) SPD; on the left panels the horizontal component (geometrical mean), on the right boards the vertical component. Thin red and black lines show the related standard deviation.

## Supplementary Files

This is a list of supplementary files associated with this preprint. Click to download.

- [Electronicsupplement.docx](#)